Materials and Structures (2024) 57:234
https://doi.org/10.1617/s11527-024-02511-x

ORIGINAL ARTICLE

The effect of quartz on natural fluorapatite decomposition during the preparation of calcium sulfoaluminate-based multiphase composites

Zeyneb Hammou · Hocine Belhouchet

Received: 21 August 2024 / Accepted: 2 November 2024

Abstract In the research described in this paper, we prepared low-cost multiphase composites based on calcium sulfoaluminate (also known as ye'elimite) and fluorapatite. By utilizing the CaO originally present in fluorapatite, the sintering densification of these composites was enhanced. The influence of varying the SiO_2 content (0–5.4 wt.%) on the reactive sintering of fluorapatite, bauxite, and gypsum was investigated. Incorporating quartz led to the formation of various compositions, including calcium hexaluminate, fluorapatite, ye'elimite, and gehlenite. Quantitative phase analysis, conducted using the Rietveld method via Profex software at various sintering temperatures, demonstrated a relationship between quartz content and the preferential formation of gehlenite over ye'elimite within the 1300–1350 °C range. Additionally, the microstructure of the composites was significantly modified by quartz addition, leading to the development of hexagonal and circular grains after heat treatment at 1400 °C.

Z. Hammou (✉)
Laboratory of Physics and Chemistry of Materials, Faculty of Sciences, University of M'sila, University Pole, Road Bourdj Bou Arreiridj, 28000 M'sila, Algeria
e-mail: zeyneb.hammou@univ-msila.dz

Z. Hammou · H. Belhouchet
Physics Department, Faculty of Sciences, University of M'sila, University Pole, Road Bourdj Bou Arreiridj, 28000 M'sila, Algeria
e-mail: hocine.belhouchet@univ-msila.dz

Published online: 18 November 2024

Keywords Fluorapatite · Ye'elimite · Gehlenite · Calcium sulfoaluminate · Quartz

Abbreviations

C	CaO
A	Al_2O_3
$	SO_3
$\overline{C}$	CO_2
S	SiO_2
H	H_2O
P	P_2O_5

1 Introduction

The cement industry, particularly the production of Portland cement, is a major contributor to CO_2 emissions, which has led to increased research into more environmentally friendly alternatives [1, 2]. Calcium sulfoaluminate (CSA) cement ($Ca_4Al_6O_{12}(SO_4)$ or $C_4A_3\$$ in cement notation) is an alternative to traditional Portland cement and is produced by burning limestone, bauxite, and gypsum to form ye'elimite [3, 4]. Recent studies on ye'elimite formation have provided valuable insights into its synthesis and applications in high-performance cementitious materials for construction. Researchers have explored various phases and microstructures during different stages of formation, thereby enhancing the understanding of raw material interactions and potentially leading to more efficient calcium sulfoaluminate cement

production process [5–8]. El-Khessaimi et al. [9] specifically examined the mechanisms underlying ye'elimite formation, utilizing advanced techniques such as X-ray diffraction (XRD), scanning electron microscopy (SEM), and thermogravimetric analysis (TGA) to analyze its complex synthesis pathways, thus providing a comprehensive understanding of this process. Although CSA cement production still releases CO_2, it offers potential for overall emission reductions compared to traditional cement [7, 10, 11]. Researchers are also exploring the use of non-carbonated calcium sources in cement production, despite challenges like scarcity and higher costs [7]. Natural fluorapatite ($Ca_5(PO_4)_3F$), the main component of natural phosphate, is considered a potential alternative raw material in cement production [11, 12], driven by the need for more sustainable materials and its abundance in the world [13, 14]. The $Ca_5(PO_4)_3F$ is gaining attention as a sustainable alternative to traditional cement raw materials due to its high calcium oxide (CaO) content and thermal stability up to 1400 °C [15–17]. This material could replace limestone in the production of ye'elimite, potentially reducing CO_2 emissions, with estimates ranging from nearly zero for volcanic phosphates to 6% for some sedimentary deposits. Algeria, particularly in the region of Djebel El-Onk in Tebessa, eastern Algeria, possesses significant natural fluorapatite reserves [18]. In 2019, the region produced approximately 1.2 million metric tons of fluorapatite, supporting the cement industry's sustainable practices [14]. Sedimentary carbonate-fluorapatite (francolite) deposits, with only around 6 wt.% CO_2 compared to limestone's 44 wt.%, offer environmental advantages for cement production [17, 19]. Boughanmi et al. [17] found that adding 0–15 wt.% natural fluorapatite to Portland cement clinker enhances cement properties, improving strength development, reducing heat evolution during hydration, and increasing sulfate resistance. These benefits highlight fluorapatite's potential to enhance performance and durability in cement-based materials, making its influence on mineral formation and composition a significant area of study in cement production and material science [20–22]. The effect of natural fluorapatite on the mineral formation and composition of cement clinker is an important area of study in the fields of cement production and material science: Djouallah et al. [18] explored the impact of alumina content on sintering fluorapatite composites from natural phosphate and alumina, finding that impurities like sulfur trioxide promoted ye'elimite formation. Ye'elimite content increased with temperature, reaching 31.9 wt.% at high temperatures with 15 wt.% Al_2O_3. Wu et al. [23] examined the effects of phosphate impurities in phosphogypsum-based ye'elimite cement production, using fluorapatite and sulfuric acid as the sole CaO source, as shown in Eq. (1). The study examined the effects of three phosphorus compounds on calcium sulfate decomposition, phase formation, and the resulting cement's hydration behavior and mechanical properties. This research provides critical insights into the role of phosphorus compounds in the mineralogical development and performance characteristics of phosphogypsum-based ye'elimite cement.

$$Ca_5(PO_4)_3F + 10H_2O + 5H_2SO_4 \rightarrow^{Heat} 3H_2PO_4 + 5\,CaSO_4.2H_2O + HF \quad (1)$$

Yao et al. [24] investigated the utilization of phosphogypsum as the exclusive CaO source in the synthesis of sulfoaluminate cement, focusing on the impact of fluoride impurities on clinker formation and the properties of the resulting cement. This study provides insights into how fluoride impurities influence phase development, hydration characteristics, and mechanical performance, contributing to a deeper understanding of phosphogypsum's viability as a sustainable CaO source in sulfoaluminate cement production. Li et al. [25] optimized the production process of belite-sulfoaluminate cement by incorporating phosphate rock acid-insoluble residue (PAIR) as the primary silica source, facilitating the complete formation of essential mineral phases. The study precisely determined an optimal temperature range for the formation of ye'elimite to be between 1150 and 1350 °C, providing valuable parameters for enhancing the synthesis efficiency and phase stability of belite-sulfoaluminate cement.

This research presents a study on developing a novel protocol for producing multi-phase composites based on ye'elimite, wherein natural fluorapatite serves as a substitute for limestone. This process investigates the impact of temperature (ranging from 1200 to 1500 °C) and varying amounts of natural quartz (up to 5.4% SiO_2) on the thermal stability and reactivity of fluorapatite, as well as the formation of other phases, including calcium hexaluminate,

ye'elimite, gehlenite, and beta-tricalcium phosphate. Using techniques such as XRD, SEM, and FT-IR, the study analyzes the microstructure, phase transformations, and material properties of the resulting composites. The findings contribute to ongoing research on environmentally friendly cement alternatives and provide insights into the formation mechanisms of key phases in calcium sulfoaluminate cement production using natural phosphate materials.

2 Materials and methods

2.1 Materials and samples synthesis

In this work, a raw mixture was used to prepare calcium hexaluminate-fluorapatite-ye'elimite-gehlenite composites from natural materials, including fluorapatite from Djebel El-Onk (Tebessa, eastern Algeria). Gypsum and quartz were sourced from Bousaâda (southeast Algeria), and bauxite was obtained from Trefisoud (El-Eulma, eastern Algeria). The chemical composition of the raw materials was determined using X-ray fluorescence. While the mineralogical composition of the natural materials was assessed via X-ray diffraction, as illustrated in Table 1 and Fig. 1. The raw materials were mixed with different amounts of quartz, i.e., 0%, 2.1%, 3.8%, and 5.4% by weight, and subsequently named M-0Q, M-2.1Q, M-3.8Q, and M-5.4Q, respectively. The amounts of raw materials used for the synthesized samples are listed in Table 2.

The powder preparation involved wet milling of the raw materials using zirconia pellets, 4–5 mm in diameter, mixed with distilled water. The mass of the material was set to one-tenth of the pellets' mass, maintaining a (1/10 ratio). The raw materials were ground for 2 h at a rotation speed of 700 rpm using an attritor-stirred ball mill machine (model JM-1) [26]. After the milling process was completed, the mixture was dried at 120 °C for 24 h, then manually ground using a mortar. It was then sieved through a 160 µm mesh to obtain a powder with particle sizes smaller than 160 µm. Subsequently, the powders were subjected to uniaxial pressure at 100 MPa to create disc-shaped samples with a diameter of 13 mm. These samples were then subjected to sintering at various temperatures (1200, 1300, 1350, 1400, and 1500 °C) for 2 h with a heating rate of 10 °C/min.

2.2 Characterization methods

The raw material composition was determined using X-ray fluorescence XRF analysis, specifically the S8 TIGER Series (Bruker, Germany). The particle size of the different powders after grinding was measured with laser granulometry with the Mastersizer 3000 (Malvern Panalytical, UK). To identify the phases, present in the powders and sintered samples, X-ray diffraction (XRD) analysis (Malvern Panalytical, UK) was conducted using CuKα radiation at 40 kV and 30 mA, with a scanning speed of 4°/min and a step scan of 0.026, covering the range from 10 to 55 degrees. All phases were identified by comparing the XRD patterns of the samples with the database from the Joint Committee on Powdered Diffraction Standards (JCPDS). Additionally, Fourier transform infrared spectroscopy (FT-IR) spectra were recorded using a Cary 630 KBr Engine from Agilent Technologies in the USA with the wave number range of 4000–400 cm^{-1}. Differential thermal analysis (DTA) experiments were performed from room temperature up to 1350 °C. The samples were heated at 10 °C/min using equipment (LABSYS EVO DTA/DSC-TG, Setaram).

The open porosity and apparent density of the sintered samples were measured using Archimedes' method of using xylene solvent. The hardness testing of the sintered samples was performed using a Vickers microhardness test (Zwick-Roell, ZHV, Germany) under a load of 300 g and a dwell time of 10 s. To

Table 1 Chemical composition (wt.%) of the fluorapatite, bauxite, gypsum and quartz used in this study

	SiO_2	Al_2O_3	Fe_2O_3	CaO	MgO	SO_3	K_2O	Na_2O	P_2O_5	TiO_2	F	LOI
Fluorapatite	2.49	0.34	0.28	49.03	1.29	2.22	0.088	0.93	28.7	0.034	3.63	10.73
Bauxite	4.96	87.7	1.95	0.301	0.30	0.18	0.73	0.03	0.073	3.96	–	–
Gypsum	0.075	0.037	0.055	33.05	0.05	45.11	–	–	0.092	0.011	–	21.01
Quartz	98.73	0.53	0.18	0.48	0.004	0.079	0.209	–	0.018	0.058	–	–

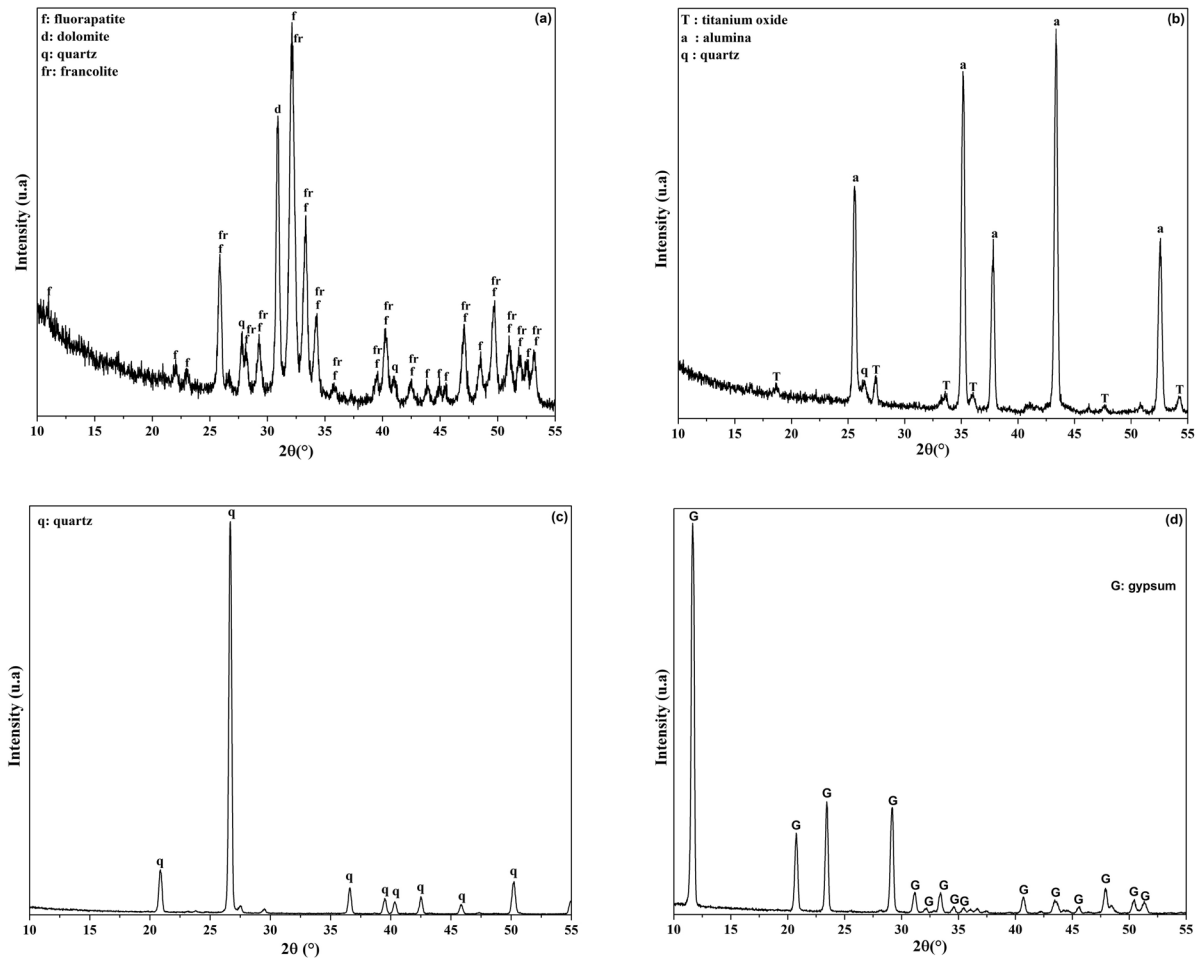

Fig. 1 XRD patterns of raw materials: **a** natural fluorapatite, **b** bauxite, **c** quartz, and **d** gypsum used in this study

Table 2 Amounts (wt.%) of the initial raw mixtures

Samples name	Fluorapatite	Bauxite	Gypsum	Quartz
M-0Q	43.20	44.50	22.10	0
M-2.1Q	46.67	40.76	20.24	2.1
M-3.8Q	49.62	37.61	18.68	3.8
M-5.4Q	52.13	34.91	17.33	5.4

calculate the average hardness value, six measurements were conducted for each shape and thickness of samples and then calculated using the provided equation [27]:

$$\mathrm{Hv} = 1.854P/d^2 \quad (2)$$

where P is the applied load in (N) and d is the diagonal length in (mm). To examine the microstructure of the sintered samples, a scanning electron microscopy analysis (SEM) is carried out using the SEM Quattro S model, (Thermo Scientific, USA).

3 Results and discussion

3.1 Phases' behavior after the grinding and drying process

Figure 2 illustrates the XRD patterns of the milled powders, which largely contain phases similar to those present in the raw materials. However, in certain mixtures, a new phase of bassanite ($CaSO_4$.1/2

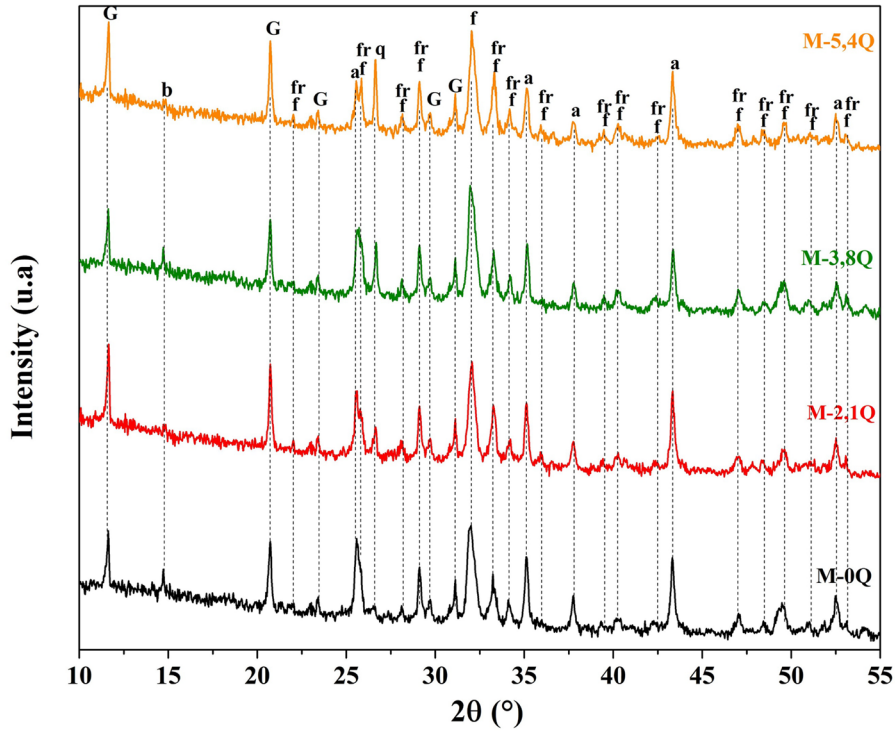

Fig. 2 XRD patterns of milled powders (G: gypsum, b: basanite, a: alumina f: fluorapatite, fr: francolite, q: quartz)

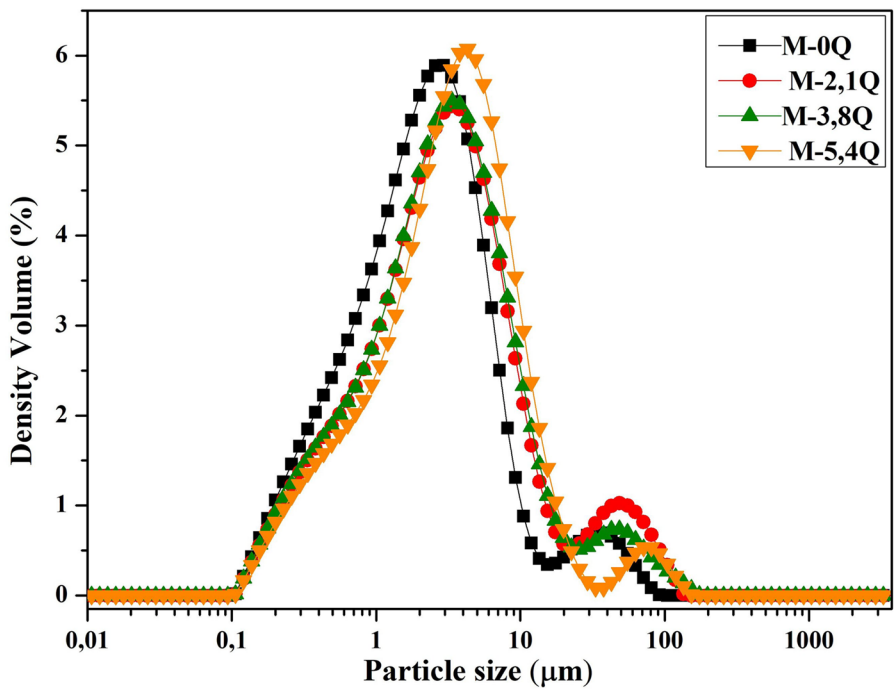

Fig. 3 Particle size distribution of milled powders

H_2O) appears in small amounts in the samples, likely due to the impact of drying temperature on gypsum [28]. Particle size analysis of the milled composite powders, as shown in Fig. 3, suggests that the milling process results in a bimodal particle size distribution. The majority of particles fall within the smaller size range, centered around a primary peak of 1–10 µm. However, a notable portion is also present in a secondary peak above 100 µm, indicating the presence of larger particles or agglomerates in some samples.

3.2 Comprehensive phases characterization and thermal analysis

DTA was used on the samples to investigate the thermal phenomena during the sintering process. The obtained DTA curves are illustrated in Fig. 4. The first endothermic peak in zone 1, occurring at around 135 °C, corresponds to the loss of water (H_2O) due to the dehydration of gypsum, as indicated by reactions (3) and (4) [5, 28]. Below endothermic peak, observed at approximately 850 °C in zone 2, is attributed to the decarbonization of francolite $Ca_{10}(PO_4, CO_3)_6F_2$ [12, 29]. In zone 3, endothermic peaks appear between 1100 and 1200 °C, accompanied by the release of outgassing (SO_2 and O_2), which can be explained by the decomposition of $CaSO_4$ [5] according to reaction (5). The exothermic peak observed between 1250 and 1350 °C (in zone 4) is due to the formation of $C_4A_3\$$. The presence of Al_2O_3 and SiO_2 can explain this, as they reduce the initial decomposition temperature of $CaSO_4$, leading to different effects on calcium-based desulfurization, which contributes to lowering calcium hexaluminate and promoting the formation of calcium sulfoaluminate in M-0Q and M-5.4Q. Two exothermic peaks belonging to ye'elimite and gehlenite were also observed in mixtures M-2.1Q, M-3.8Q, and M-5.4Q, resulting from interactions between the interphases represented by SiO2, CaO, and Al2O3, which XRD of the samples explains at 1300–1350 °C [30–32]. The formation of ye'elimite can be attributed to solid-state reactions between CaO, Al_2O_3, and $CaSO_4$, according to Eqs. (6) and (7) [3]:

$$CaSO_4 \cdot 2H_2O \rightarrow CaSO_4.1/2\ H_2O + 3/2\ H_2O \uparrow \quad (3)$$

$$CaCO_4 \cdot 1/2H_2O \rightarrow CaSO_4 + 1/2H_2O \uparrow \quad (4)$$

$$CaSO_4 \rightarrow CaO + 1/2\ O_2 \uparrow + SO_2 \uparrow \quad (5)$$

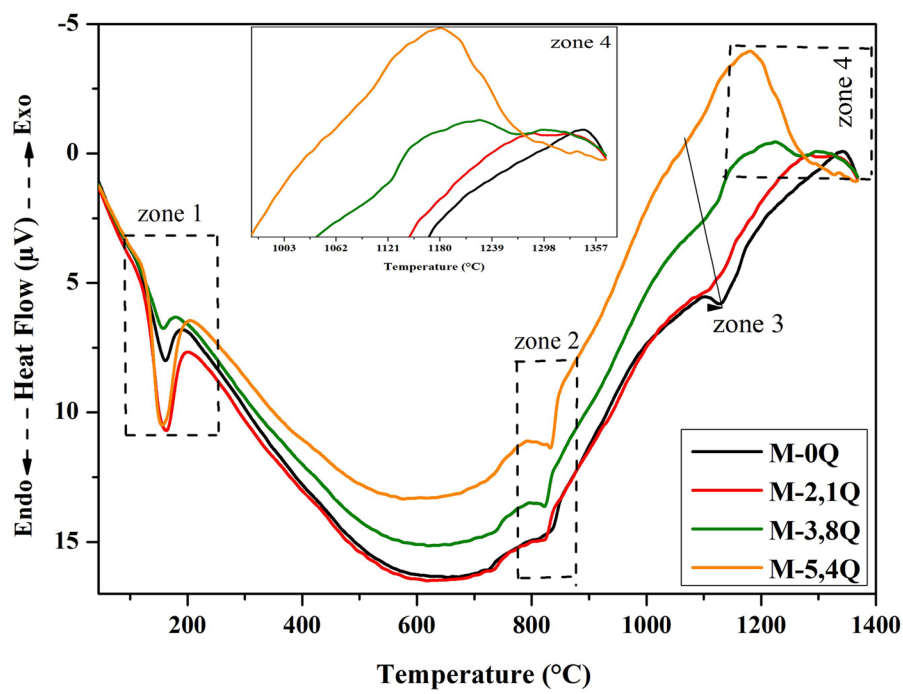

Fig. 4 DTA curves of the raw mixture during heating process

$$4CaO + 3Al_2O_3 + SO_3 \rightarrow Ca_4(AlO_2)_6SO_4 \quad (6)$$

$$3CaO + 3Al_2O_3 + CaSO_4 \rightarrow Ca_4(AlO_2)_6SO_4 \quad (7)$$

The XRD patterns of samples sintered at the various temperatures are shown in Fig. 5. At 1200 °C, the main phases are fluorapatite, alumina, and ye'elimite in all samples, with a small amount of wollastonite ($CaSiO_3$) in mixtures containing quartz due to the reaction between the free calcium oxide and silicon dioxide, as according to Eq. (8) [33]:

$$CaO + SiO_2 \rightarrow CaSiO_3 \quad (8)$$

The significant decrease in the intensity of the diffraction peaks corresponding to the ye'elimite phase in M-2.1Q and M-3.8Q samples at 1300–1350 °C can be attributed to the reaction between the SiO_2 and Al_2O_3 ratios, which affects the initial decomposition temperature of $CaSO_4$. Consequently, this ratio had clear effects on the desulfurization process. The reaction between quartz and ye'elimite led to the formation of intermediate phases or solid solutions during sintering [34]. These phases affect the nucleation and growth behavior of the ye'elimite crystals by changing the chemical composition and diffusion paths within the material. The competition between gehlenite ($Ca_2Al_2SiO_7$, CA_2S) and ye'elimite depends on the availability of aluminum and calcium ions, as both require these ions for their formation. When quartz

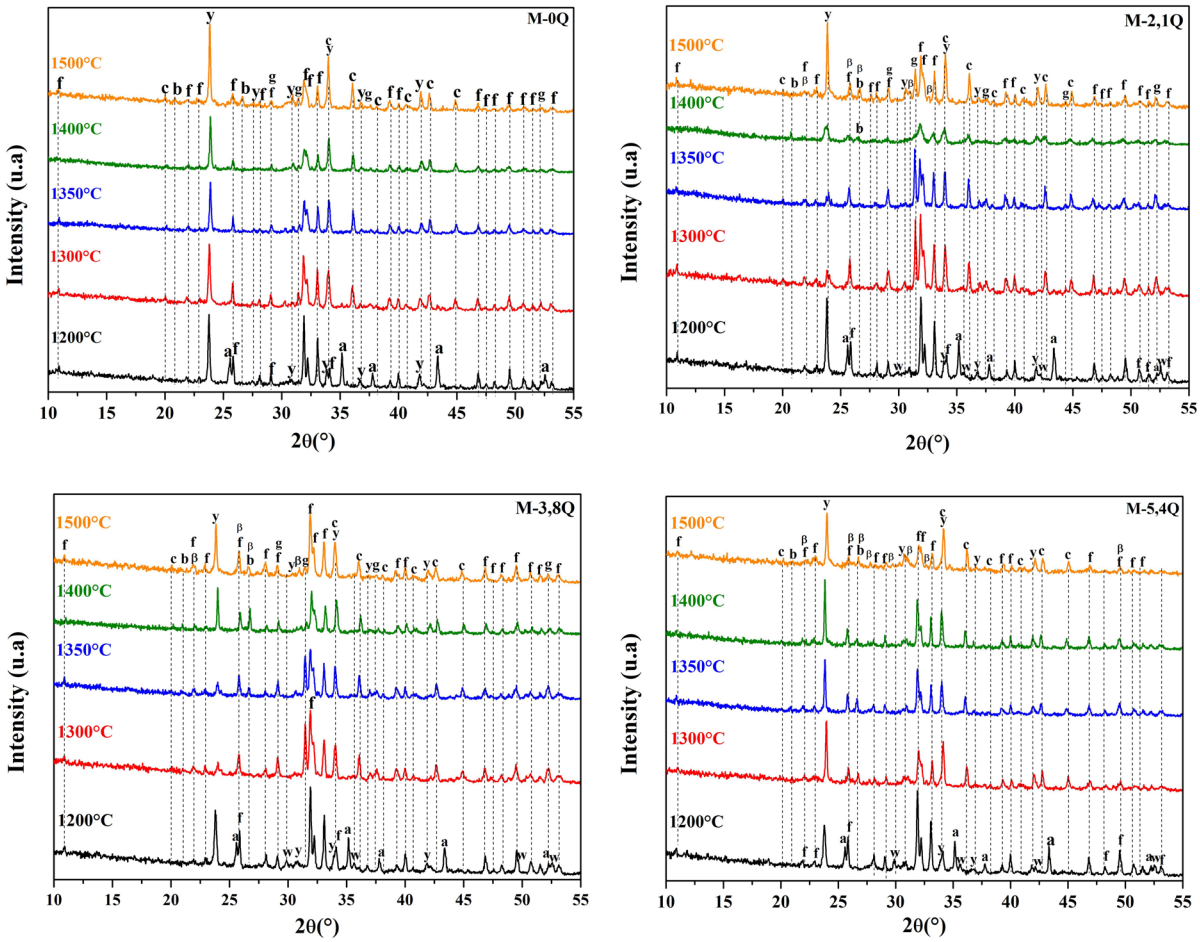

Fig. 5 XRD analysis of sintered samples at different temperatures: a: alumina f: fluorapatite, c: calcium hexaluminate, y: ye'elimite, g: gehlenite, b: berlinite, β: β-TCP

is present in large amounts, it can consume available ions, reducing the amount available for ye'elimite formation and potentially favoring other phases [32, 35]. During sintering at 1300–1350 °C, gehlenite can compete with ye'elimite for the available aluminum (Al) and calcium (Ca) ions. This competition reduces the amount of these crucial components available for ye'elimite formation, leading to a lower concentration of ye'elimite in the final product. This particular factor stands as the primary explanation for the different findings reported by various researchers [36–38]. This competition for ions may suppress or delay the crystallization of ye'elimite, ultimately affecting the phase composition and microstructure of the final material, as shown in Eqs. (9) and (10) [39]:

$$2CaO + Al_2O_3 + SiO_2 \rightarrow Ca_2Al_2SiO_7 \quad (9)$$

$$4SiO_2 + 2Ca_4Al_6O_{12}(SO_4) \rightarrow 2Al_2O_3 + 4Ca_2Al_2SiO_7 + O_2 \uparrow + 2SO_2 \uparrow \quad (10)$$

We also noticed a contrasting relationship between C_2AS and $C_4A_3\$$, as shown in Fig. 4. It can act as a catalyst or inhibitor of $C_4A_3\$$ formation, depending on the specific reaction pathways involved. In some cases, C_2AS may enhance the nucleation and growth of $C_4A_3\$$ crystals by providing suitable nucleation sites or facilitating the transport of reactants. Conversely, C_2AS may also compete with $C_4A_3\$$ for available aluminum and calcium ions, which may prevent its formation under certain conditions of sintering temperature and quartz ratios [30, 35, 39]. On the other hand, we noticed the formation of calcium hexaluminate ($CaAl_{12}O_{19}$, CA_6). This phase transitions through various intermediate phases within the CaO-Al_2O_3 system. The most significant phases in calcium aluminate compounds include $CaAl_2O_4$, $CaAl_4O_7$, and $CaAl_{12}O_{19}$, which were present in all samples due to the interaction between Al_2O_3 and CaO [38]:

$$CaO + Al_2O_3(s) \rightarrow CaAl_2O_4 \quad (11)$$

$$CaAl_2O_4 + Al_2O_3(s) \rightarrow CaAl_4O_7 \quad (12)$$

$$CaAl_4O_7 + 4\ Al_2O_3 \rightarrow CaAl_{12}O_{19} \quad (13)$$

The reactions between Al_2O_3 and $Ca_4Al_6O_{12}(SO_4)$ are also possible, resulting in the formation of calcium hexaluminate ($CaAl_{12}O_{19}$) [18]:

$$21Al_2O_3 + Ca_4Al_6O_{12}(SO_4) \rightarrow 4CaAl_{12}O_{19} + SO_3 \quad (14)$$

As the sintering temperature was raised to 1400–1500 °C, the peaks of the ye'elimite phase became sharper. This was the result of the dissociation of the fluorapatite phase, driven by the presence of free CaO and P_2O_5. Simultaneously, a portion of the dissociated fluorapatite transformed into beta-tricalcium phosphate (β-TCP) and also contributed to the formation of the berlinite ($AlPO_4$) phases [40]:

$$Ca_{10}(PO_4)_6F_2 + 3Al_2O_3 \rightarrow 6AlPO_4 + 9CaO + CaF_2 \quad (15)$$

$$P_2O_5 + Al_2O_3 \rightarrow 2AlPO_4 \quad (16)$$

The potential reactions linked to the dissociation of fluorapatite can be outlined as follows [41]:

$$Ca_{10}(PO_4)_6F_2 \rightarrow 3Ca_3(PO_4)_2 + CaF_2 \quad (17)$$

$$Ca_{10}(PO_4)_6F_2 + H_2O \rightarrow 3Ca_3(PO_4)_2 + Ca_4(PO_4)_2O + 2HF \quad (18)$$

$$3Ca_{10}(PO_4)_6F_2 \rightarrow 2Ca_3(PO_4)_2 + 6Ca_4(PO_4)_2O + 2\ POF_3 \quad (19)$$

Figure 6 illustrates the FT-IR spectra of the samples sintered at various temperatures. Irrespective of the amount of quartz present, the absorption peaks at 1093 and 1036 cm^{-1} were consistently detected, corresponding to the asymmetric stretching vibration (ν_3) mode of the PO_4^{3-} group in fluorapatite [42, 43]. Additional peaks associated with the vibration modes (ν_4) of PO_4^{3-} were also identified at 602 and 562 cm^{-1} [44–46]. In addition, the vibration mode (ν_1) of PO_4^{3-} was evident at 960 cm^{-1} [16]. The intensity of the (ν_3) peaks of the PO_4^{3-} group decreased with increasing quartz content and sintering temperature. This phenomenon is supported by XRD findings, which indicate the partial decomposition of fluorapatite, as observed in this research [16, 18, 43, 47, 48], as shown by reactions (16), (17), and (18). On the other hand, peaks related to Al-O bonds 640 cm-1 [45], Ca-O–Al or Al–O–Al groups (840, 890, and 919 cm^{-1}) [49, 50], and Si–O-Al or Si–O-Si groups (491, 698, 767, and 1147 cm^{-1}) [51], were also

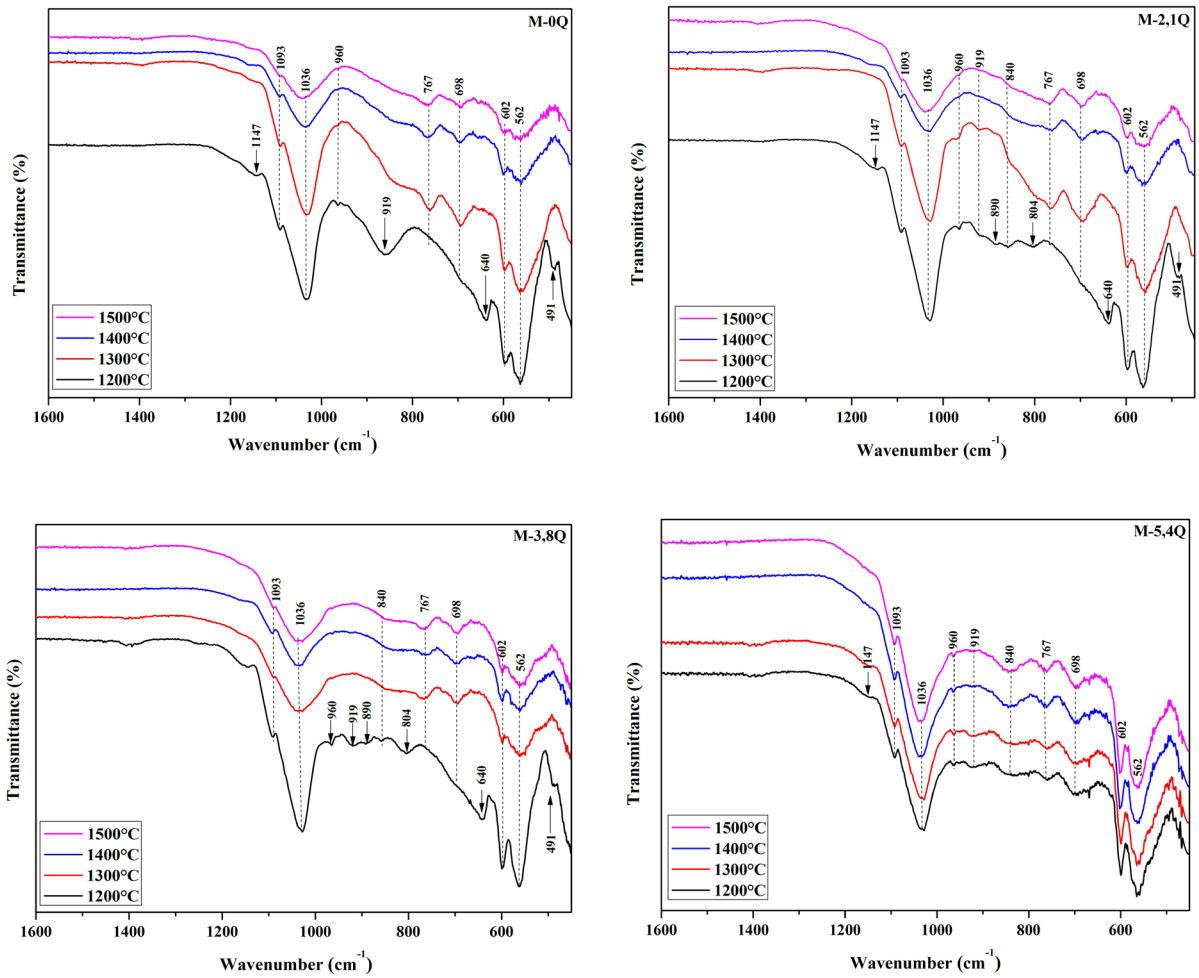

Fig. 6 FT-IR spectrum of sintered samples sintered at various temperatures

observed, supporting the XRD detection of alumina, calcium aluminate compounds, and silicate phases like gehlenite. In the samples M-2.1Q and M-3.8Q sintered at 1200°C, there was evidence of symmetric Si–O-Si stretching modes of the SiO_4 tetrahedron in the range of 804 cm^{-1}. This may be due to the formation of calcium silicate phases, such as wollastonite, as supported by the XRD identification [52]. Both analyses revealed compositional and structural changes with increasing temperature and quartz content. FTIR provided insights into chemical bonds and functional groups, complementing the crystalline phase data from XRD.

Table 3 ICSD codes and chemical formula for phases mineral

Mineral phase	Chemical formula	ICSD code
Fluorapatite	$Ca_5(PO_4)_3F$	015 – 0876
Alumina	Al_2O_3	042 – 1468
Ye'elimite	$Ca_4Al_6O_{12}(SO_4)$	016 – 0440
Gehlenite	$Ca_2Al_2SiO_7$	035 – 0755
Calcium hexaluminate	$CaAl_{12}O_{19}$	038 – 0470
Berlinite	$AlPO_4$	076 – 0228
β-TCP	$Ca_3(PO_4)_2$	009 – 0169
Wollastonite	$Ca_6Si_6O_{18}$	043 – 1460

3.3 Quantitative phase analysis and microstructural examination

The crystal structures, based on the XRD patterns, are provided in Table 3. It gives the nomenclatures, chemical formulas, and ICSD card numbers of the mineral phases contained in the sintered samples. These results present quantitative phase analysis data obtained through the Rietveld method using Profex software, as shown in Fig. 7 [53, 54]. The quantitative phase analysis of the XRD patterns provides comprehensive validation of the qualitative observations, offering deeper insights into the complex phase transformations occurring during sintering at various temperatures and quartz contents.

At 1200 °C, the dominance of fluorapatite (43.94–51.01 wt.%), alumina (22.25–34.16 wt.%), and ye'elimite (15.66–21.9 wt.%) is confirmed, with wollastonite present only in quartz-containing samples (2.1, 3.8, and 5.4 wt.% SiO_2), aligning with the reaction in Eq. (7). The dramatic decrease in ye'elimite content (down to 0.36–2.85 wt.%) and the increase in gehlenite (up to 19.83–20.44 wt.%) at 1300–1350 °C in the quartz-rich samples, as shown in Fig. 7b, c, quantitatively support the XRD observed competition between these phases for Al and Ca ions [27]. This competition is particularly evident in the inverse relationship between ye'elimite and gehlenite contents, confirming the reactions described in Eqs. (8) and (9) [38]. The formation of calcium hexaluminate

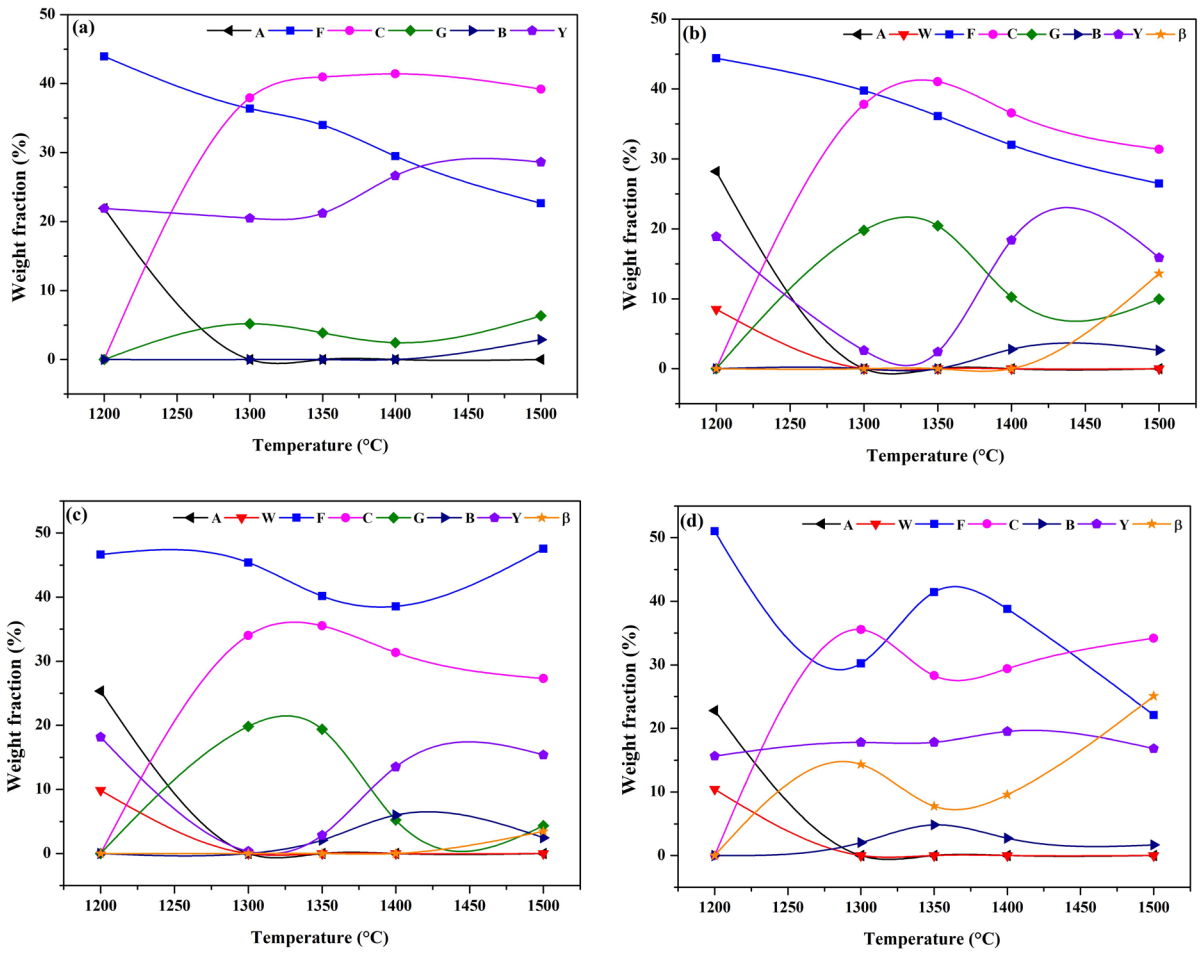

Fig. 7 Weight fraction of phases content as a function of quartz addition and sintering temperature: **a** M-0Q, **b** M-2.1Q, **c** M-3.8Q and **d** M-5.4Q (A: alumina, F: fluorapatite, C: calcium hexaluminate, Y: ye'elimite, (G): gehlenite, B: berlinite, β: β-TCP, W: wollastonite)

(34–41.06 wt.%) across this temperature range aligns with the XRD detected CaO-Al_2O_3 system phases, supporting the reactions in Eqs. (10–13) [36, 56]. At 1400–1500 °C, the quantitative data confirm the XRD results, showing sharper ye'elimite peaks (rising to 13.51–28.63 wt.%), fluorapatite dissociation (dropping to 22.1 wt.% in Fig. 7d at 1500 °C), and the formation of β-TCP and berlinite (0–6.01 wt.%) [18, 57, 58]. The complete decomposition of gehlenite in Fig. 7d at 1500 °C, accompanied by increases in ye'elimite (16.83 wt.%) and calcium hexaluminate (34.19 wt.%), further validates the XRD observations of phase transformations at high temperatures [23]. These results demonstrate the critical influence of quartz content and temperature on phase formation and stability, particularly for ye'elimite and gehlenite, which significantly impact the material's properties and performance [35, 55]. The quantitative data also highlight the importance of maintaining specific Al_2O_3 and SiO_2 ratios (between 2 and 4 wt.% SiO_2) and sintering temperatures (1300–1350 °C) to optimize ye'elimite content, as excessive gehlenite formation can negatively impact hydraulic activity and overall performance, as noted by previous researchers [30, 39].

Figure 8 shows the SEM micrographs of multi-phase-based composite samples. We observed clear microstructural evolution across the samples sintered at 1400 °C for 2 h, revealing distinct microstructural changes correlated with increasing quartz content, which aligns with the quantitative phase analysis and XRD results. Figure 8a displays a dense structure with small, rounded particles, likely indicative of ye'elimite grains [24, 58, 59]. As observed in Fig. 8b, the microstructure becomes more porous with the presence of larger, irregular particles, suggesting the onset of liquid phase formation [18]. Figure 8c, d reveal a dramatic shift towards prominent hexagonal sheet-like structures, characteristic of calcium hexaluminate crystal. This transformation aligns with the reported effects of increasing quartz content and higher sintering temperatures [60]. The hexagonal

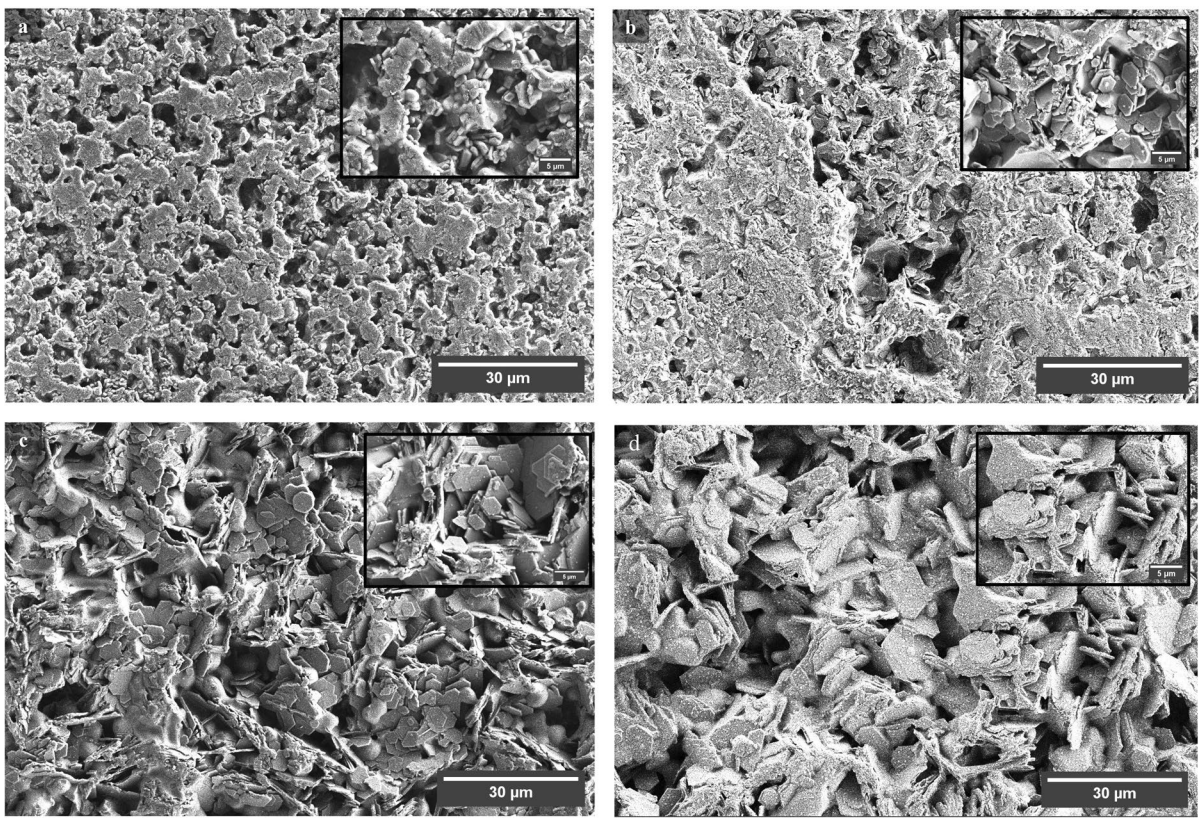

Fig. 8 SEM micrographs of fracture surface of sample: **a** M-0Q, **b** M-2.1Q, **c** M-3.8Q and **d** M-5.4Q sintered at 1400 °C

sheet-like structures in Fig. 8d appear more defined and thicker than in Fig. 8c. This observation correlates with the XRD data showing high calcium hexaluminate content (34–41.06 wt.%) at this temperature [18, 61]. This detailed correlation between the SEM observations and XRD results at 1400 °C elucidates the intricate relationships between composition, phase evolution, and resulting microstructure in this complex ceramic system. It highlights how the sintering process and quartz content at this specific temperature influence the final material properties [62].

3.4 Evaluating the impact of porosity on sintered sample properties

The variations in open porosity and bulk density of the samples with sintering temperature were determined using Archimedes' principle. The results are shown in Fig. 9. In general, it was observed that as the sintering temperature increased up to 1400 °C, the bulk density of the samples increased, while the open porosity decreased in all samples. For samples M-0Q, M-2.1Q, and M-3.8Q, the bulk density remained relatively constant within the temperature range of 1200 to 1300 °C. However, sample M-5.4Q, it exhibits a linear increase, reaching a value of 2.85 ± 0.11 g/cm^3 at 1300 °C (Fig. 9a). Furthermore, the noticeable increase in bulk density was evident in the temperature range from 1300 to 1400 °C for these samples. At 1400 °C, all mixtures achieve relatively high densities, with values for samples M-0Q, M-2.1Q, M-3.8Q, and M-5.4Q ranging from 1.65 to 2.8 g/cm^3. In general, we support that the formation of both calcium hexaluminate and gehlenite phases was responsible for this increasing density, as corroborated by the XRD patterns [36]. However, the lower bulk density of 2.62 g/cm^3 observed in sample M-5.4Q when sintered at 1500°C can be explained by a combination of increased trapped pores (from gas evolution during sintering) and thermal expansion, both of which are significantly affected by the sample's higher quartz content at this temperature [18].

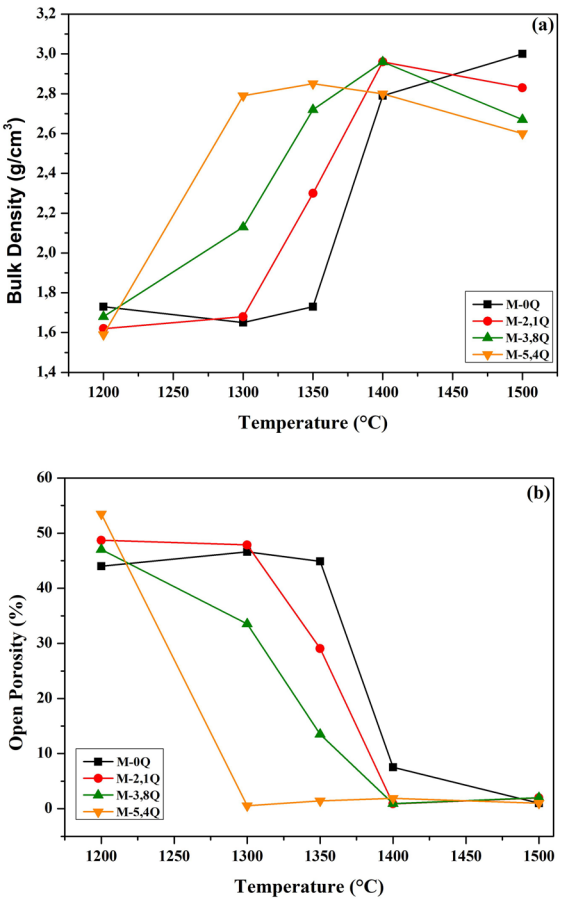

Fig. 9 Effect of sintering temperatures on the **a** bulk density and **b** open porosity of heated samples

Open porosity is an important parameter that needs to be considered in the cement industry. This can be beneficial for cement manufacturers, as the porous material allows clinker to be easily ground into cement. The value of the open porosity was practically constant between 33.5 and 48.7% in the temperature range from 1200 to 1300 °C, not for M-5.4Q (Fig. 9b). A linear decrease in open porosity values from 53.5 to 0.5% was observed for sample M-5.4Q. At higher temperatures (1300–1400 °C), a gradual and regular decrease in open porosity values was noted. The reduction of open porosity can be explained by the release of large amounts of sulfur dioxide and oxygen gas at these temperatures. Above 1400 °C, the open porosity remained relatively stable, being nearly constant in the temperature range between 1400 and 1500 °C. Vickers hardness measurements were conducted on the dense samples sintered at 1400 °C, as shown in Table 4. Regardless of quartz addition, the hardness values ranged from 3.54 to 6.13 GPa, suggesting no clear correlation between the hardness of the samples and their density [57].

Table 4 The bulk density and Vickers hardness of samples sintered at 1400 °C

Samples	M-0Q	M-2.1Q	M-3.8Q	M-5.4Q
Bulk density (g/cm^3)	2.79 ± 0.11	2.96 ± 0.12	2.96 ± 0.12	2.66 ± 0.10
Vickers hardness (GPa)	3.54 ± 0.14	5.63 ± 0.22	5.78 ± 0.23	6.13 ± 0.24

4 Conclusions

Our research demonstrates the feasibility of manufacturing diverse composites based on calcium hexaluminate-fluorapatite-ye'elimite-gehlenite from natural fluorapatite (as an alternative to limestone), bauxite, and gypsum. A thorough analysis of ye'elimite-based multiphase composites reveals intricate connections among sintering temperature, quartz content, and phase formation. The milling process had minimal impact on the initial powder phases, while the thermal analysis identified key reactions, including gypsum dehydration, carbonate-fluorapatite decarbonation, and $CaSO_4$ decomposition. As the sintering temperatures increased from 1200 to 1500 °C, complex phase transformations occurred, forming ye'elimite, calcium hexaluminate, gehlenite, at higher temperatures, β-TCP and berlinite. The amount of quartz addition critically influenced these transformations, with an optimal range of 2–4 wt.% at 1300–1350 °C maximizing the ye'elimite content. However, excess quartz promoted gehlenite formation, potentially compromising the cement performance. The physical properties improved with sintering, showing increased bulk density (up to 2.95 g/cm^3) and decreased open porosity (as low as 0.5%) at 1400 °C. The sample without quartz (M-0Q) exhibited a uniform distribution of spherical-shaped grains throughout the matrix, indicative of ye'elimite phase formation. In contrast, the quartz-containing samples showed altered microstructures, demonstrating the role of quartz in modifying the material's composition and properties. Vickers hardness values ranged from 3.54 to 6.13 GPa for the samples sintered at 1400 °C.

The study also highlighted the role of the quartz addition, which significantly contributed to the decomposition of fluorapatite, especially at higher sintering temperatures. This was evidenced by the FT-IR spectra analysis, which showed a decrease in the intensity of the (PO_4^{3-}) group peaks with increasing quartz content and sintering temperature. We believe these detailed findings provide crucial insights for optimizing ye'elimite-based multiphase composites, allowing for tailored properties to meet specific requirements in the construction industry and for heat-resistant materials.

Declarations

Conflict of interest No potential conflict of interest was reported by the authors.

References

1. Goyal S, Sharma D (2020) CO2 sequestration on cement. Elsevier Ltd., Amsterdam
2. Shi C, Qu B, Provis JL (2019) Recent progress in low-carbon binders. Cem Concr Res 122:227–250. https://doi.org/10.1016/j.cemconres.2019.05.009
3. Pimraksa K, Chindaprasirt P (2018) Sulfoaluminate cement-based concrete. Elsevier Ltd, Amsterdam
4. Zea-Garcia JD, Santacruz I, Aranda MAG, De la Torre AG (2019) Alite-belite-ye'elimite cements: effect of dopants on the clinker phase composition and properties. Cem Concr Res 115:192–202. https://doi.org/10.1016/j.cemconres.2018.10.019
5. El Khessaimi Y, El Hafiane Y, Smith A et al (2018) Solid-state synthesis of pure ye'elimite. J Eur Ceram Soc 38:3401–3411. https://doi.org/10.1016/j.jeurceramsoc.2018.03.018
6. Bullerjahn F, Scholten T, Scrivener KL et al (2020) Formation, composition and stability of ye'elimite and iron-bearing solid solutions. Cem Concr Res 131:106009. https://doi.org/10.1016/j.cemconres.2020.106009
7. El Khessaimi Y, Taha Y, El Mahdi Safhi A et al (2022) Synthesis of MgO-belite calcium sulfoaluminate cement from phosphate mine waste rock and phosphogypsum. In: Material today proceedings, 58:1081–1090. https://doi.org/10.1016/j.matpr.2022.01.136
8. Abir FZ, Mesnaoui M, Abouliatim Y et al (2022) Effect of the addition of iron oxide on the microstructure of ye'elimite. Cem Concr Res 151:106625. https://doi.org/10.1016/j.cemconres.2021.106625
9. El Khessaimi Y, El Hafiane Y, Smith A (2019) Examination of ye'elimite formation mechanisms. J Eur Ceram Soc 39:5086–5095. https://doi.org/10.1016/j.jeurceramsoc.2019.07.042
10. Miller SA, John VM, Pacca SA, Horvath A (2018) Carbon dioxide reduction potential in the global cement industry by 2050. Cem Concr Res 114:115–124. https://doi.org/10.1016/j.cemconres.2017.08.026

11. Bahhou A, Taha Y, El Khessaimi Y et al (2020) Use of phosphate mine by-products as supplementary cementitious materials. In: Material today proceedings, 37:3781–3788. https://doi.org/10.1016/j.matpr.2020.07.619
12. Tkalčec E, Popović J, Orlić S et al (2014) Hydrothermal synthesis and thermal evolution of carbonate- fluorhydroxyapatite scaffold from cuttlefish bones. Mater Sci Eng C 42:578–586. https://doi.org/10.1016/j.msec.2014.05.079
13. Cooper J, Lombardi R, Boardman D, Carliell-Marquet C (2011) The future distribution and production of global phosphate rock reserves. Resour Conserv Recycl 57:78–86. https://doi.org/10.1016/j.resconrec.2011.09.009
14. Boumaza B, Kechiched R, Chekushina TV (2021) Trace metal elements in phosphate rock wastes from the Djebel Onk mining area (Tébessa, eastern Algeria): a geochemical study and environmental implications. Appl Geochem 127:104910. https://doi.org/10.1016/j.apgeochem.2021.104910
15. Belhouchet H, Chouia F, Hamidouche M, Leriche A (2016) Preparation and characterization of anorthite and hydroxyapatite from Algerian kaolin and natural phosphate. J Therm Anal Calorim 126:1045–1057. https://doi.org/10.1007/s10973-016-5655-8
16. Kenzour A, Belhouchet H, Kolli M et al (2019) Sintering behavior of anorthite-based composite ceramics produced from natural phosphate and kaolin. Ceram Int 45:20258–20265. https://doi.org/10.1016/j.ceramint.2019.06.299
17. Boughanmi S, Labidi I, Megriche A et al (2018) Natural fluorapatite as a raw material for Portland clinker. Cem Concr Res 105:72–80. https://doi.org/10.1016/j.cemconres.2018.01.006
18. Djouallah S, Belhouchet H, Kenzour A, Kherifi D (2021) Sintering behavior of fluorapatite-based composites produced from natural phosphate and alumina. Ceram Int 47:3553–3564. https://doi.org/10.1016/j.ceramint.2020.09.202
19. Supriya CR, Sharma U et al (2023) Low-CO2 emission strategies to achieve net zero target in cement sector. J Clean Prod 417:137466. https://doi.org/10.1016/j.jclepro.2023.137466
20. Xie L, Deng M, Tang J, Liu K (2021) The effect of fluorapatite in limestones on the mineral compositions of Portland cement clinkers. Constr Build Mater 273:122042. https://doi.org/10.1016/j.conbuildmat.2020.122042
21. Liu S, Ouyang J, Ren J (2020) Mechanism of calcination modification of phosphogypsum and its effect on the hydration properties of phosphogypsum-based supersulfated cement. Constr Build Mater 243:118226. https://doi.org/10.1016/j.conbuildmat.2020.118226
22. Caponero J, Tenório JAS (2000) Laboratory testing of the use of phosphate-coating sludge in cement clinker. Resour Conserv Recycl 29:169–179. https://doi.org/10.1016/S0921-3449(99)00040-3
23. Wu S, Yao X, Yao Y et al (2022) Recycling phosphogypsum as the sole calcium oxide source in calcium sulfoaluminate cement production and solidification of phosphorus. Sci Total Environ 808:152118. https://doi.org/10.1016/j.scitotenv.2021.152118
24. Yao X, Wu S, Ren C, Wang W (2024) Preparing sulfoaluminate cement using phosphogypsum as the only calcium oxide source: effects of fluoride impurities. Constr Build Mater 416:135296. https://doi.org/10.1016/j.conbuildmat.2024.135296
25. Li R, He W, Zhang J et al (2022) Preparation of belite–sulphoaluminate cement using phosphate rock acid-insoluble residue. Constr Build Mater 323:126573. https://doi.org/10.1016/j.conbuildmat.2022.126573
26. El-Eskandarany MS (2015) Mechanical alloying: nanotechnology, materials science and powder metallurgy
27. Belhouchet K, Bayadi A, Belhouchet H, Romero M (2019) Improvement of mechanical and dielectric properties of porcelain insulators using economic raw materials. Bol la Soc Esp Ceram y Vidr 58:28–37. https://doi.org/10.1016/j.bsecv.2018.05.004
28. Krejsová J, Kužel R, Keppert M et al (2024) New insight into the phase changes of gypsum. Mater Struct Constr 57:1–17. https://doi.org/10.1617/s11527-024-02404-z
29. Antonakos A, Liarokapis E, Leventouri T (2007) Micro-Raman and FTIR studies of synthetic and natural apatites. Biomaterials 28:3043–3054. https://doi.org/10.1016/j.biomaterials.2007.02.028
30. Berrio A, Tobón JI, De la Torre AG (2022) Kinetic model for ye'elimite polymorphs formation during clinkering production of CSA cement. Constr Build Mater. https://doi.org/10.1016/j.conbuildmat.2022.126336
31. Ptáček P, Opravil T, Šoukal F et al (2013) Kinetics and mechanism of formation of gehlenite, Al-Si spinel and anorthite from the mixture of kaolinite and calcite. Solid State Sci 26:53–58. https://doi.org/10.1016/j.solidstatesciences.2013.09.014
32. Yan Z, Wang Z, Liu H et al (2015) Decomposition and solid reactions of calcium sulfate doped with SiO2, Fe2O3 and Al2O3. J Anal Appl Pyrolysis 113:491–498. https://doi.org/10.1016/j.jaap.2015.03.019
33. Böhme N, Hauke K, Neuroth M, Geisler T (2019) In situ Raman imaging of high-temperature solid-state reactions in the CaSO4–SiO2 system. Int J Coal Sci Technol 6:247–259. https://doi.org/10.1007/s40789-019-0252-7
34. Ben Haha M, Winnefeld F, Pisch A (2019) Advances in understanding ye'elimite-rich cements. Cem Concr Res 123:105778. https://doi.org/10.1016/j.cemconres.2019.105778
35. Berrio A, Rodriguez C, Tobón JI (2018) Effect of Al2O3/SiO2 ratio on ye'elimite production on CSA cement. Constr Build Mater 168:512–521. https://doi.org/10.1016/j.conbuildmat.2018.02.153
36. Bai P, Chai Y, Qiu Y et al (2014) The effect of sintering temperature on prepared and properties of calcium hexaluminate/gehlenite composites. Sci Sinter 46:315–321. https://doi.org/10.2298/SOS1403315B
37. Pan X, Zhang D, Wu Y, Yu H (2018) Synthesis and characterization of calcium aluminate compounds from gehlenite by high-temperature solid-state reaction. Ceram Int 44:13544–13550. https://doi.org/10.1016/j.ceramint.2018.04.186
38. Sahu S, Majling J (1993) Phase compatibility in the system CaOSiO2Al2O3Fe2O3SO3 referred to sulphoaluminate belite cement clinker. Cem Concr Res 23:1331–1339. https://doi.org/10.1016/0008-8846(93)90070-P

39. Arjunan P, Silsbee MR, Roy DM (1999) Sulfoaluminate-belite cement from low-calcium fly ash and sulfur-rich and other industrial by-products. Cem Concr Res 29:1305–1311. https://doi.org/10.1016/S0008-8846(99)00072-1
40. Jumas JC, Goiffon A, Capelle B et al (1987) Crystal growth of berlinite, AlPO4: physical characterization and comparison with quartz. J Cryst Growth 80:133–148. https://doi.org/10.1016/0022-0248(87)90533-1
41. Nasiri-Tabrizi B, Fahami A (2013) Reaction mechanisms of synthesis and decomposition of fluorapatite-zirconia composite nanopowders. Ceram Int 39:5125–5136. https://doi.org/10.1016/j.ceramint.2012.12.008
42. Ben AF, Bouaziz J (2008) Sintering of tricalcium phosphate-fluorapatite composites by addition of alumina. Ceram Int 34:1885–1892. https://doi.org/10.1016/j.ceramint.2007.07.017
43. Mezahi FZ, Oudadesse H, Harabi A et al (2009) Dissolution kinetic and structural behaviour of natural hydroxyapatite vs. thermal treatment: comparison to synthetic hydroxyapatite. J Therm Anal Calorim 95:21–29. https://doi.org/10.1007/s10973-008-9065-4
44. Agathopoulos S, Tulyaganov DU, Marques PAAP et al (2003) The fluorapatite-anorthite system in biomedicine. Biomaterials 24:1317–1331. https://doi.org/10.1016/S0142-9612(02)00468-4
45. Boumaza A, Favaro L, Lédion J et al (2009) Transition alumina phases induced by heat treatment of boehmite: an x-ray diffraction and infrared spectroscopy study. J Solid State Chem 182:1171–1176. https://doi.org/10.1016/j.jssc.2009.02.006
46. Azami M, Jalilifiroozinezhad S, Mozafari M, Rabiee M (2011) Synthesis and solubility of calcium fluoride/hydroxy-fluorapatite nanocrystals for dental applications. Ceram Int 37:2007–2014. https://doi.org/10.1016/j.ceramint.2011.02.025
47. Mezahi FZ, Oudadesse H, Harabi A, Le Gal Y (2012) Effect of ZrO2, TiO2, and Al2O3 additions on process and kinetics of bonelike apatite formation on sintered natural hydroxyapatite surfaces. Int J Appl Ceram Technol 9:529–540. https://doi.org/10.1111/j.1744-7402.2011.02742.x
48. Merzougui M, Mezahi FZ, Dakhouche A et al (2022) Improvement of the reactivity of triethyl phosphate and structural behavior of hydroxyapatite versus the synthesis conditions by sol–gel route. Chem Pap 76:1045–1061. https://doi.org/10.1007/s11696-021-01938-8
49. Tian Y, Pan X, Yu H, Tu G (2016) Formation mechanism of calcium aluminate compounds based on high-temperature solid-state reaction. J Alloys Compd 670:96–104. https://doi.org/10.1016/j.jallcom.2016.02.059
50. Kim SJ, Bang HG, Song JH, Park SY (2009) Effect of fluoride additive on the mechanical properties of hydroxyapatite/alumina composites. Ceram Int 35:1647–1650. https://doi.org/10.1016/j.ceramint.2008.07.016
51. Rafienia M, Bigham A, Saudi A, Rahmati S (2018) Gehlenite nanobioceramic: sol-gel synthesis, characterization, and in vitro assessment of its bioactivity. Mater Lett 225:89–92. https://doi.org/10.1016/j.matlet.2018.04.094
52. Mahdy MA, El Zawawi IK, Kenawy SH et al (2022) Effect of zinc oxide on wollastonite: structural, optical, and mechanical properties. Ceram Int 48:7218–7231. https://doi.org/10.1016/j.ceramint.2021.11.282
53. Doebelin N, Kleeberg R (2015) Profex: a graphical user interface for the Rietveld refinement program BGMN. J Appl Crystallogr 48:1573–1580. https://doi.org/10.1107/S1600576715014685
54. Döbelin N, Archer R, Tu V (2022) A free and open-source solution for rietveld refinement of XRD data from the CheMin instrument onboard the mars rover curiosity. Planet Space Sci. https://doi.org/10.1016/j.pss.2022.105596
55. Wang Z, Li J, Huang S et al (2022) Effect of Al2O3/SiO2 ratio on the chroma and phase compositions of white sulfoaluminate cement clinker. Constr Build Mater 345:128202. https://doi.org/10.1016/j.conbuildmat.2022.128202
56. Leite A, Costa G, Hajjaji W et al (2009) Blue cobalt doped-hibonite pigments prepared from industrial sludges: formulation and characterization. Dye Pigment 81:211–217. https://doi.org/10.1016/j.dyepig.2008.10.008
57. Li H, Wang R, Zhao W et al (2022) Sintered glass-ceramic foams from fluorite tailings and waste glass with calcium phosphate addition. Constr Build Mater 359:129528. https://doi.org/10.1016/j.conbuildmat.2022.129528
58. Li R, Zhang J, He W et al (2023) Preparation of belite-sulfoaluminate cement with phosphate-rock acid-insoluble residue: modification and influence of impurity ions on cement properties. Constr Build Mater 365:130077. https://doi.org/10.1016/j.conbuildmat.2022.130077
59. Abir FZ, El Hafiane Y, Smith A et al (2023) Chemical synthesis and crystallographic data on iron doped cubic ye'elimite. Cem Concr Res. https://doi.org/10.1016/j.cemconres.2023.107257
60. Khajornboon J, Ota K, Washijima K, Shiono T (2018) Control of hexagonal plate-like microstructure of in-situ calcium hexaluminate in monolithic refractories. J Asian Ceram Soc 6:196–204. https://doi.org/10.1080/21870764.2018.1484621
61. Pieta A, Bućko MM, Januś M et al (2015) Calcium hexaaluminate synthesis and its influence on the properties of CA2-Al2O3-based refractories. J Eur Ceram Soc 35:4567–4571. https://doi.org/10.1016/j.jeurceramsoc.2015.08.034
62. Chouia F, Belhouchet H, Sahnoune F, Bouzrara F (2015) Reaction sintering of kaolin-natural phosphate mixtures. Ceram Int 41:8064–8069. https://doi.org/10.1016/j.ceramint.2015.03.003